J. Plasma Phys. (2026), *vol*. 92, E14 © The Author(s), 2026. Published by Cambridge University Press.
This is an Open Access article, distributed under the terms of the Creative Commons Attribution licence (https://creativecommons.org/licenses/by/4.0/), which permits unrestricted re-use, distribution and reproduction, provided the original article is properly cited. doi:10.1017/S0022377825101062

Plasma rotation driven by lasers with zero angular momentum

Camilla Willim[1], Thales Silva[1], Luís O. Silva[1] and Jorge Vieira[1]

[1]GoLP/Instituto de Plasmas e Fusão Nuclear, Instituto Superior Técnico, Universidade de Lisboa, 1049-001 Lisbon, Portugal

Corresponding author: Camilla Willim, camillawillim@googlemail.com, camilla.willim@u-bordeaux.fr

(Received 15 February 2025; revision received 8 November 2025; accepted 9 November 2025)

We present a novel mechanism in which plasma electrons and ions optically acquire angular momentum during local pump depletion of an azimuthally polarised laser, despite the laser carrying none. Using theoretical considerations and multi-dimensional particle-in-cell simulations, we find that this process is enabled by a strong frequency downshift at the gradually eroding laser pulse front. We further show that the angular momentum gained by the plasma electrons is compensated by the ions and by the combined electromagnetic fields of the laser and nonlinear plasma wave. By varying key laser parameters such as phase, frequency and polarisation, we demonstrate that the transverse momentum of high-energy electrons can be effectively controlled.

Key words: plasma nonlinear phenomena, plasma simulation, plasma waves

1. Introduction

The transfer of optical angular momentum plays a critical role in diverse research areas, ranging from the precise control of nanoparticle motion (Porfirev, Khonina & Kuchmizhak 2023) to the generation of substantial axial magnetic fields (Talin, Kaftandjian & Klein 1975; Najmudin *et al*. 2001; Shi *et al*. 2018), the development of compact accelerators for twisted electron beams with relativistic energies (Vieira, Mendonça & Quéré 2018) and the emission of radiation with angular momentum from the spiral motion of high-energy electrons (Seipt, Surzhykov & Fritzsche 2014; Katoh *et al*. 2017; Luís Martins *et al*. 2019).

Optical angular momentum transfer in underdense plasmas has been studied in the context of the inverse Faraday effect, which was initially explored using circularly polarised lasers (Talin *et al*. 1975; Sheng & Meyer-ter Vehn 1996; Gorbunov & Ramazashvili 1998; Haines 2001; Kostyukov *et al*. 2001; Najmudin *et al*. 2001; Frolov 2004; Naseri, Bychenkov & Rozmus 2010; Liu, Jia & Zheng 2023). Later studies included lasers with orbital angular momentum (Allen *et al*. 1992), relying on the direct absorption of laser angular momentum (Ali, Davies & Mendonca 2010; Nuter *et al*. 2020; Longman & Fedosejevs 2021). Moreover, angular momentum transfer to plasma waves and energetic charged particles has been

https://doi.org/10.1017/S0022377825101062 Published online by Cambridge University Press

demonstrated using lasers with orbital angular momentum (Baumann & Pukhov 2018), spatio-temporally coupled beams forming light springs (Vieira *et al*. 2018) and twisted beat waves (Saberi, Vieira & Silva 2017; Shi *et al*. 2018).

So far, optically induced plasma electron rotation has primarily been associated with circularly polarised lasers and lasers with orbital angular momentum. These lasers exhibit distinct types of angular momentum – spin and orbital – which enable the angular motion of electrons through direct absorption or higher-order nonlinearities (Sheng & Meyer-ter Vehn 1996; Haines 2001; Frolov 2004). The time-averaged angular momentum density of an electromagnetic wave is given by $\langle \mathcal{L} \rangle = 1/(4\pi c)\boldsymbol{r} \times \langle \boldsymbol{E} \times \boldsymbol{B} \rangle$, where $\boldsymbol{E}$ and $\boldsymbol{B}$ are the electric and magnetic field vectors, expressed in Gaussian CGS units, and c is the speed of light. A laser beam carries angular momentum when the time-averaged momentum density $1/(4\pi c)\langle \boldsymbol{E} \times \boldsymbol{B} \rangle$ has an azimuthal component.

Here, we demonstrate that the plasma can gain angular momentum from lasers without angular momentum, such as azimuthally polarised lasers. Azimuthally polarised laser pulses consist of two orthogonally polarised transverse electromagnetic (TEM_{01}) modes, i.e. $\mathrm{TEM}_{01(x)}\hat{e}_y - \mathrm{TEM}_{01(y)}\hat{e}_x$ (Nesterov & Niziev 2000; Oron *et al*. 2000). At focus, the vector potential is described by $\boldsymbol{A}(r) = a_0(r/w_0)\exp(-r^2/w_0^2)\hat{e}_\theta$, where w_0 is the beam waist and $\hat{e}_\theta = -\sin\theta\hat{e}_x + \cos\theta\hat{e}_y$ is the unit vector in polar direction with $\theta = \tan^{-1}(y/x)$. This configuration exhibits a hollow intensity profile and corresponds to a transverse electric (TE) mode, featuring an electric field component, E_θ, oriented in polar direction and perpendicular to the propagation direction, with radial B_r and axial B_z components of the magnetic field. As a result, its time-averaged momentum density is directed along the z-axis, $1/(4\pi c)\langle \boldsymbol{E} \times \boldsymbol{B} \rangle = 1/(4\pi c)\langle E_\theta B_r \rangle \hat{e}_z$, similar to radial polarisation and linearly polarised Gaussian beams (Volke-Sepulveda *et al*. 2002). Therefore, these lasers have zero angular momentum density and thus have not been previously associated with optically induced electron rotation.

Through analytical considerations and one- and three-dimensional particle-in-cell (PIC) simulations using OSIRIS (Fonseca *et al*. 2002), we show that plasma rotation arises from canonical momentum conservation and is facilitated by a non-vanishing vector potential that trails the main laser pulse, a phenomenon that develops during local pump depletion (Decker *et al*. 1996). We further demonstrate the conservation of total angular momentum and that the mechanism can be tuned, mainly through the laser polarisation and the laser-to-plasma frequency ratio.

In the following, we normalise the electric $\boldsymbol{E}$ and magnetic fields $\boldsymbol{B}$ to $m_e c\omega_p/e$. The vector potential A is normalised to $m_e c/e$, where the dimensionless vector potential is given by $a_0 = eA/m_e c$. Distances $\boldsymbol{x}$, velocity v, and time t are normalised to c/ω_p, c and $1/\omega_p$, respectively. The plasma frequency is defined as $\omega_p = \sqrt{4\pi n_e e^2/m_e}$, where n_e is the background plasma density and m_e is the electron mass.

2. One-dimensional analysis of local pump depletion and transverse momentum gain of electrons

It is instructive to review the self-consistent laser-plasma dynamics in one dimension to study how the mechanism works. We simulate an ultra-intense short laser pulse with a dimensionless amplitude $a_0 = 6$ ($I \approx 8 \times 10^{19}$ W cm^{-2}) and full-width at half-maximum (FWHM) pulse duration $\tau = 3/\omega_p$ ($\sim$10 fs). The laser is linearly polarised (in y-direction) with a central frequency $\omega_0 = 8\,\omega_p$. Initially, the

https://doi.org/10.1017/S0022377825101062 Published online by Cambridge University Press

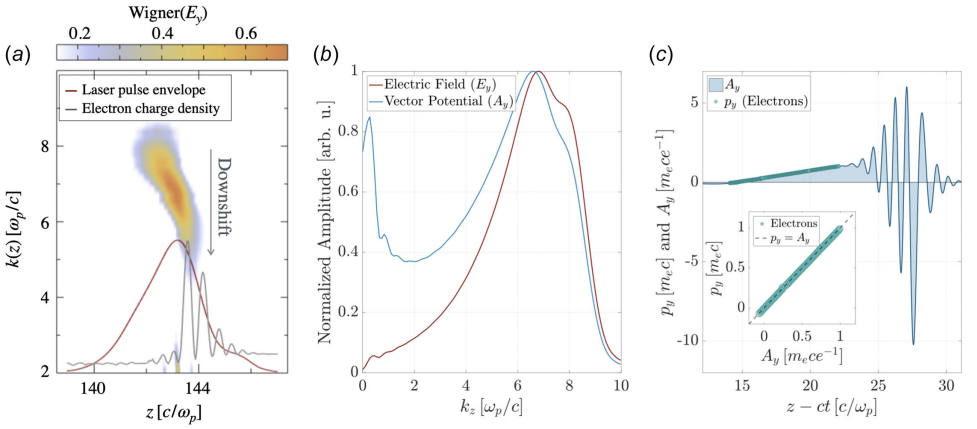


FIGURE 1. One-dimensional OSIRIS simulation results at time $t \approx 116/\omega_p$ showcase the frequency downshift of the laser electric field E_y, which manifests in the vector potential A_y amid local pump depletion, enabling the plasma electrons to acquire transverse momentum in the nonlinear wakefield behind the main laser pulse. (*a*) Frequency of the laser electric field (envelope of E_y in red) dropping at the leading edge (Wigner distribution of E_y), which resides in a steep electron charge density spike (grey line). (*b*) Normalised amplitude of the low k-spectrum of the vector potential A_y (blue line) surpassing that of the laser's electric field $E_y = -\partial A_y/\partial t$ (red line). (*c*) Vector potential A_y (blue line) exhibiting a long wavelength offset trailing the laser pulse ($(z - ct) \lesssim 25\, c/\omega_p$ in the co-moving frame), where the electrons acquire transverse momentum, following canonical momentum conservation $p_y = A_y$ (highlighted in the inset).

laser pulse's vector potential $\boldsymbol{A}$ vanishes (nearly zero) outside the laser pulse. The underdense plasma starts at $z = 34\, c/\omega_p$ and is homogeneous with a density of $n_e = 1/64\, n_{cr} \approx 2.7 \times 10^{19}$ cm^{-3}, where $n_{cr} \approx 1.7 \times 10^{21}$ cm^{-3} corresponds to the critical density for a laser wavelength of $\lambda = 800$ nm. The ions are assumed to be static. The simulation is performed in a moving window that travels at the speed of light c. The simulation box is $68\, c/\omega_p$ long, divided into 6800 cells and one particle per cell.

Figure 1 illustrates how local pump depletion enables the plasma electrons to acquire transverse momentum in a nonlinear wakefield behind the main laser pulse. This process is driven by a localised frequency downshift at the high-intensity laser pulse front (figure 1*a*), the formation of a long-wavelength offset in the laser's vector potential (figure 1*b*), which manipulates the electrons' transverse momentum through canonical momentum conservation (figure 1*c*).

The laser pulse front pushes electrons away from regions of high intensity, thereby modifying the refractive index through electron density modulation and relativistic mass increase, $\eta = \sqrt{1 - \omega_p^2/(\omega^2\gamma)}$, where $\gamma = \sqrt{1 + a^2/2}$ for a linearly polarised laser (Esarey *et al*. 1996). This interaction ensures that the laser front continuously encounters a positive gradient of the refractive index, $\partial\eta/\partial\xi$, where $\xi = t - z/c$ is the speed of light variable. As a result, the laser frequency (and thus the axial wavenumber k_z) shifts down via phase modulation (Mendonça & Silva 1994; Silva & Mendonça 1998, 2001), where the frequency change can be described by $(1/\omega)(\partial\omega/\partial t) = -(1/c)(\eta^{-2})(\partial\eta/\partial\xi)$ (Mori 1997; Tsung *et al*. 2002). The plasma frequency ω_p marks the smallest frequency that can propagate. This localised frequency downshift is observable in the Wigner transform of the laser's electric field E_y in figure 1(*a*). The position of the frequency downshift overlaps with the electron

https://doi.org/10.1017/S0022377825101062 Published online by Cambridge University Press

density spike (grey line) and the steepened leading edge of the laser pulse's electric field (envelope in red line) (Silva & Mendonça, 2001; Vieira *et al*. 2010).

The frequency downshift manifests in an increase of the vector potential, which acquires a substantial long-wavelength offset while the electric field appears eroded (Bulanov *et al*. 1992; Decker *et al*. 1996; Tsung *et al*. 2002). This is due to the conservation of the total wave action, $\mathcal{N} \sim |A_y|^2\omega = \text{constant}$ (Bulanov *et al*. 1992; Tsung *et al*. 2002); the vector potential increases while the laser frequency decreases. As a result, the k_z-spectrum of the vector potential A_y is increased for low wavenumbers, peaking at a few of the plasma wavenumber $k_p = \omega_p/c$ (see figure 1*b*).

The longer wavelength components travel with a smaller group velocity, where the group velocity can be approximated by $v_g \simeq c(1 - \omega_p^2/(2\omega^2))$ (Mori 1997). Thus, in figure 1(*c*), we observe a long wavelength offset trailing the main part of the laser pulse. The finite vector potential behind the laser pulse gradually decreases until it vanishes at the back of the wakefield. The electrons (blue dots) acquire a finite transverse momentum $p_y = A_y$, following the conservation of canonical momentum (see inset in figure 1*c*).

This mechanism has been related to pulse compression (Silva & Mendonça 1998; Tsung *et al*. 2002; Gordon *et al*. 2003; Faure *et al*. 2005) and proposed as a diagnostic for wakefields (Dias, Silva & Mendonça 1998; Murphy *et al*. 2006; Shiraishi *et al*. 2013; Downer *et al*. 2018). In addition, the concept has been extended to explore the generation of mid-infrared to infrared pulses (Chen & Pukhov 2015; Nie *et al*. 2020; Pai *et al*. 2010; Schreiber *et al*. 2010; Zhu *et al*. 2012, 2013; Zhu *et al*. 2020) and betatron-like radiation from energetic electrons (Lu *et al*. 2021).

In this set-up, electrons can be efficiently accelerated due to the high accelerating gradients within the nonlinear wakefield, reaching gradients of GV m^{-1} (Esarey *et al*. 1996). Within short propagation distances and times, self-injected electrons become trapped in the wakefield and are accelerated to high energies ($\gtrsim$100 MeV). In figure 2(*a*), we demonstrate that in addition to their longitudinal acceleration, the high-energy electrons acquire transverse momentum. Specifically, the self-injected electrons with $p_z \gtrsim 140\, m_e c$ localised around the same axial position $(z - ct) \approx 16\, c/\omega_p$ within the nonlinear wakefield all contain similar transverse momentum $p_y \approx 0.25\, m_e c$ (highlighted in the inset of figure 2*a*).

Furthermore, during local pump depletion, the transverse momentum of the injected electrons oscillates with increasing magnitude (Nerush & Kostyukov 2009), matching the long wavelength offset of the vector potential, as shown in figures 2(*b*) and 2(*c*). The oscillation period of the long-wavelength offset of the vector potential is closely linked to the etching velocity – the rate at which the laser's leading edge erodes, defined as $v_{\text{etch}} \approx c(\omega_p^2/\omega_0^2)$ (Decker *et al*. 1996). The oscillation period can be approximated as $T \sim \lambda/v_{\text{etch}}$, where λ is the laser wavelength inside the plasma. In figure 2(*c*), we demonstrate an agreement between the oscillation of the long-wavelength offset and the erosion of the leading edge of the vector potential. The observed period of the oscillation, highlighted by dashed lines $T/2 \approx 25/\omega_p$, matches the theoretical estimate $T/2 \approx (\lambda/2) \times \omega_0^2/(c\omega_p^2) \approx (\pi/8) \times 64/\omega_p \approx 25/\omega_p$.

This section presents key results, demonstrating that the transverse momentum of plasma electrons is tuneable according to the laser's polarisation and through the laser-to-plasma frequency ratio, which governs the gradual erosion of the laser's leading edge. This enhances the control of plasma electron dynamics through the wide range of accessible laser polarisation states, e.g. linear, circular, radial, azimuthal and even spatially varying polarisation profiles.

https://doi.org/10.1017/S0022377825101062 Published online by Cambridge University Press

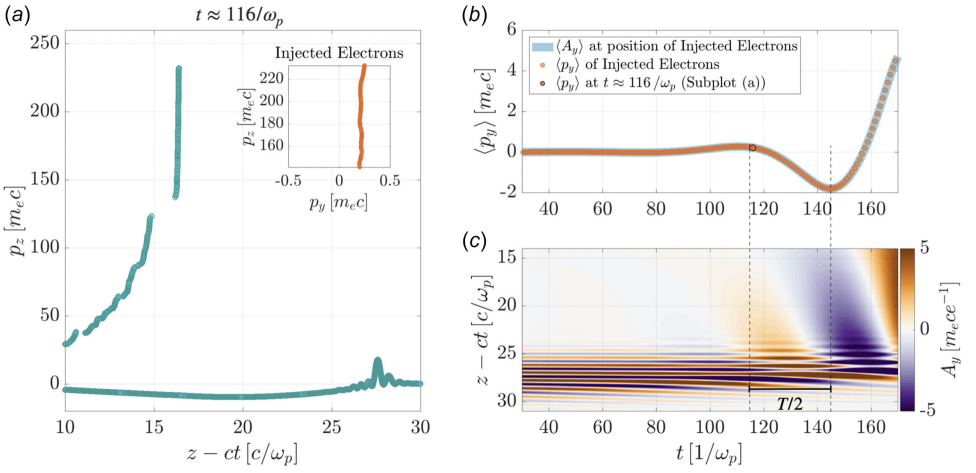


FIGURE 2. One-dimensional OSIRIS simulations show self-injected electron transverse momentum oscillations in a nonlinear wakefield, with increasing magnitude and a period linked to the laser's leading-edge erosion. (*a*) Electrons' position, $z - ct$ in the co-moving frame and longitudinal momentum, p_z, at time $\approx 116/\omega_p$, showing high-energy electrons with $p_z > 140\, m_e c$ concentrated at $(z - ct) \approx 16\, c/\omega_p$, with their transverse momentum around $p_y \approx 0.25\, m_e c$, as highlighted in the inset (orange dots). (*b*) Time evolution of the mean transverse momentum of the high-energy electrons, $\langle p_y \rangle$, represented by orange dots, aligning well with the corresponding vector potential at their position, $\langle A_y \rangle$, shown as a blue line. The black-circled position corresponds to the time step of panel (*a*). (*c*) Time evolution of the vector potential A_y in the co-moving frame illustrating the erosion of the leading edge and the development of an oscillating long-wavelength offset. The oscillation half-period, $T/2 \approx 25/\omega_p$, is highlighted by dashed lines, illustrating the connection between the erosion of the leading edge, the long-wavelength offset and the transverse momentum of the electrons shown in panel (*b*).

3. Three-dimensional analysis of angular momentum gain of electrons

Building on our one-dimensional analysis, we extend our study to three dimensions, confirming the robustness of electron transverse momentum gain. In this context, we show that plasma electrons acquire angular momentum from a high-intensity azimuthally polarised laser pulse in underdense plasma, driving a nonlinear wakefield in the bubble regime (Pukhov & Meyer-ter Vehn 2002). Figure 3 shows the angular momentum of electrons from the bubble's current sheath and injected electrons.

We simulate an azimuthally polarised laser pulse with a dimensionless amplitude of $a_0 = 6$, FWHM pulse duration $\tau = 3/\omega_p$, a central frequency $\omega_0 = 8\,\omega_p$ and a laser spot size $w_0 = 5.5\, c/\omega_p$. Considering a wavelength of $\lambda = 800$ nm, this corresponds to a laser with approximately 600 mJ, $w_0 = 5.6\,\mu$m and with pulse duration $\tau \approx 10$ fs propagating in a plasma with density $n_e = 2.7 \times 10^{19}$ cm^{-3}. The simulation is performed in a moving window that travels at the speed of light c. The simulation box has the dimensions $34 \times 34 \times 34\,(c/\omega_p)^3$, divided into $1700 \times 1700 \times 1700$ cells and 4 particles per cell.

In figure 3(*a*), we present simulation results of an azimuthally polarised laser pulse driving a doughnut-shaped plasma bubble, reflecting the laser's hollow intensity distribution (Vieira & Mendonça 2014). The electrons comprising the bubble and the self-injected electrons have angular momentum, as indicated by the arrows in blue

https://doi.org/10.1017/S0022377825101062 Published online by Cambridge University Press

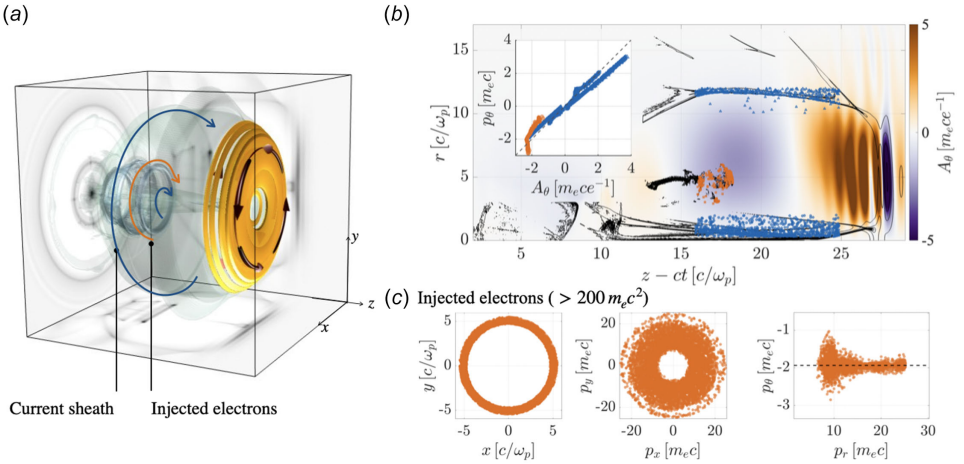


FIGURE 3. Three-dimensional OSIRIS simulation results at $t \approx 150/\omega_p$ illustrate the angular momentum gain of plasma electrons in a nonlinear wakefield, driven by an azimuthally polarised laser pulse – facilitated by the development of a long-wavelength offset in the laser's azimuthal vector potential due to local pump depletion. (*a*) Hollow intensity laser pulse (orange isosurfaces) with azimuthal polarisation (black arrows) driving a doughnut-shaped nonlinear wakefield in the bubble regime (grey isosurfaces). Projections show the spatial distribution of the electron charge density, highlighting increased density at the laser pulse front. The blue and orange arrows indicate the direction of rotation of the electrons belonging to the electron sheath comprising the doughnut-shaped bubble (blue) and the injected electrons inside the bubble (orange). The illustrated box dimensions are $20 \times 20 \times 20\ (c/\omega_p)^3$. (*b*) Vector potential A_θ (yellow–purple colourmap) exhibits a long-wavelength offset trailing the laser pulse ($z \lesssim 25\ c/\omega_p$). Electrons in the inner and outer current sheaths (blue dots) and the self-injected electrons (orange dots) acquire azimuthal momentum following canonical momentum conservation, $p_\theta = A_\theta$, (see inset). (*c*) High-energy ($>200\, m_e c^2$) injected electrons form a ring in both configuration and transverse momentum space, exhibiting a well-defined angular momentum with a mean value of $\langle p_\theta \rangle \approx -2 m_e c$ (dashed line).

and orange. Figure 3(*b*) shows the driver's vector potential at $t \approx 150/\omega_p$, undergoing local pump depletion and developing a substantial long-wavelength offset that remains confined within the bubble structure. The electrons from the inner and outer current sheaths (highlighted in blue) and the high-energy self-injected electrons (highlighted in orange) possess angular momentum in agreement with canonical momentum conservation, $p_\theta = eA_\theta$ (see inset in figure 3*b*). Here, $p_\theta = m_e \gamma r \dot{\theta}$ is the angular momentum, where $\gamma = \sqrt{1 + |\boldsymbol{p}|^2}$ is the relativistic factor, $\dot{\theta}$ is the electron's angular frequency and A_θ is the laser's azimuthal vector potential at the position of the electrons (see more on angular momentum conservation in the Appendix). In figure 3(*c*), we highlight the high-energy ($>200\, m_e c^2$) self-injected electrons, forming a ring structure in physical and transverse momentum space. The electrons carry a well-defined angular momentum, with a mean value of $\langle p_\theta \rangle \approx -2 m_e c$. The total charge of these high-energy electrons is $\approx$212 pC.

Consistent with angular momentum conservation, the angular momentum gained by the plasma electrons is compensated by the ions and by the combined electromagnetic fields of the laser and the nonlinear plasma wave. To show this, we consider

https://doi.org/10.1017/S0022377825101062 Published online by Cambridge University Press

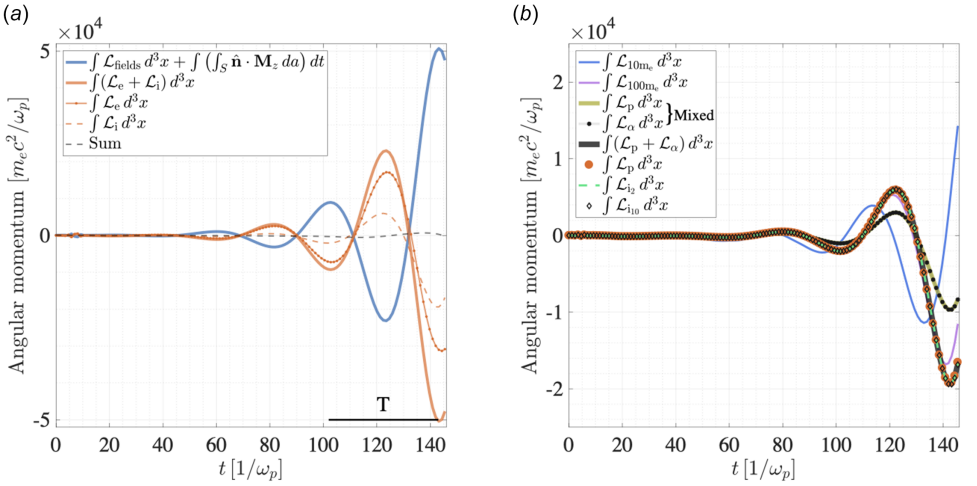


FIGURE 4. Three-dimensional OSIRIS simulation results showing the evolution of angular momentum components, as defined in (3.1). (*a*) Angular momentum gained by the plasma electrons and ions (orange line) is compensated by that of the combined wakefield and laser fields (blue line). Individual contributions from electrons and ions are indicated in orange by crosses and a dashed line. The horizontal black line labelled 'T' indicates the oscillation period. (*b*) Angular momentum acquired by protons and heavier ions is independent of their mass. This trend deviates for lighter species, as their motion influences local pump depletion and wakefield formation. We compare positively charged species with ten (blue line) and one hundred (purple line) times the electron mass, a mixed gas of protons (green line) and alpha particles (grey-dotted) and their sum (black line), protons (orange-dotted), ions with twice the proton mass (green dashed line), and ions with ten times the proton mass (black diamonds).

the integral form of the angular momentum conservation law for a closed system, without particle loss, given by (Jackson 1998)

$$\int_V (\mathcal{L}_{\text{mech}} + \mathcal{L}_{\text{field}})\ \mathrm{d}^3x + \int \left(\int_S \hat{n} \cdot \boldsymbol{M}\ \mathrm{d}a \right)\ \mathrm{d}t = 0, \tag{3.1}$$

where $\mathcal{L}_{\text{mech}} = n_e \boldsymbol{r} \times \boldsymbol{p_e} + n_i \boldsymbol{r} \times \boldsymbol{p_i}$ is the mechanical angular momentum density of the electrons and ions, and $\mathcal{L}_{\text{field}} = 1/(4\pi c)\boldsymbol{r} \times (\boldsymbol{E} \times \boldsymbol{B})$ represents the angular momentum density carried by the fields. Here, the electric and magnetic fields are the combined wakefields and laser fields. The term $\boldsymbol{M} = \boldsymbol{r} \times \boldsymbol{T}$ stands for the angular momentum flux, with $\boldsymbol{T}$ being the Maxwell stress tensor normal to the closed surface S.

Figure 4(*a*) illustrates the individual and combined angular momentum contributions from the electrons, the ions and the electromagnetic fields, as expressed in (3.1) (see supplementary movie 1 available at https://doi.org/10.1017/S002237782510 1062 for the full evolution). The mechanical angular momentum of the electrons and ions is balanced by the angular momentum of the electromagnetic fields. The electrons' angular momentum exceeds that of the ions, which can be attributed to electron accumulation in regions of enhanced vector potential, where they naturally acquire more angular momentum. Figure 4(*b*) shows that the angular momentum acquired by ions is mass independent, consistent with canonical momentum conservation, $p_\theta = -eA_\theta$. This is evident from the overlapping curves for the protons, the heavier ions and the proton–alpha mixture, with the mixture's angular

https://doi.org/10.1017/S0022377825101062 Published online by Cambridge University Press

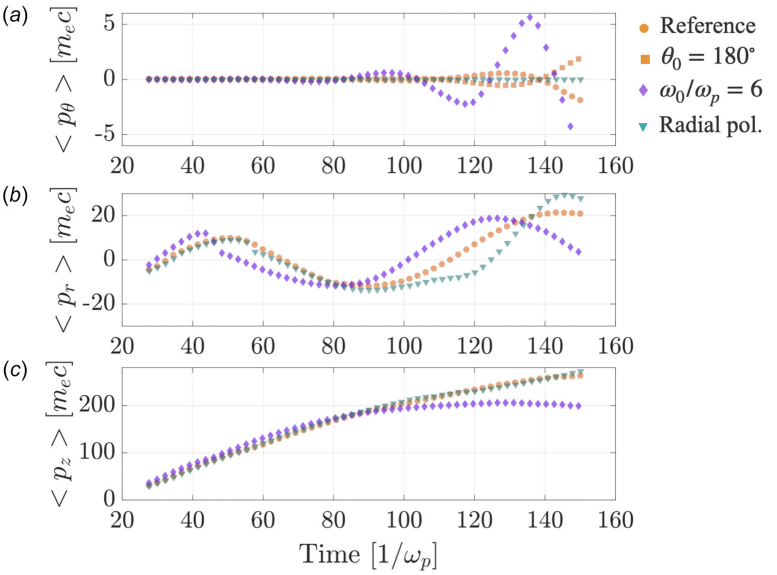


FIGURE 5. Three-dimensional OSIRIS simulation results demonstrate how adjustments of laser parameters allow for the control of angular (transverse) momentum of high-energy electrons (>80 % of the maximum energy) under local pump depletion. (*a*)–(*c*) Time evolution of the (*a*) mean azimuthal momentum $\langle p_\theta \rangle$, (*b*) mean radial momentum $\langle p_r \rangle$ and (*c*) mean longitudinal momentum $\langle p_z \rangle$ for different laser and plasma parameters. Orange dots correspond to the reference case with $\theta_0 = 0$, $\omega_0/\omega_p = 8$ and azimuthal polarisation; orange squares correspond to a change in the initial laser phase, $\theta_0 = 180°$; purple diamonds represent a change in the laser-to-plasma frequency ratio, $\omega_0/\omega_p = 6$; and blue triangles illustrate the transition to radial polarisation. Note that the phase change affects only p_θ, such that the points overlap in panels (*b*) and (*c*).

momentum dividing evenly between the two species. Only the curves for the lighter positively charged species ($10\,m_e$ and $100\,m_e$) deviate from this trend, as their motion influences local pump depletion and wakefield formation. The period of the angular momentum oscillation can be approximated as $T \sim \lambda/v_{\text{etch}}$, similar to the one-dimensional discussion around figures 2(*b*) and 2(*c*). To our knowledge, this is the first quantitative verification of angular momentum conservation in a PIC simulation.

The mechanism is robust and tuneable, primarily governed by the laser-to-plasma frequency ratio and the laser intensity, which must be sufficiently high ($a_0 > 3$, Tsung *et al*. 2002) for local pump depletion to occur. Other influencing factors include the laser phase, polarisation, chirp and pulse duration.

Figure 5 shows a parameter scan on the tunability of angular (transverse) momentum under local pump depletion, focusing on the momentum space evolution of self-injected high-energy electrons. We examine the effect of three key parameters on the high-energy electrons (>80 % of the maximum energy) – the initial phase of the laser, which we vary from $\theta_0 = 0°$ to 180° (depicted by orange squares in figure 5), the laser-to-plasma frequency ratio, which we vary from $\omega_0/\omega_p = 8$ to 6 (depicted by purple diamonds), and the laser polarisation where we change from azimuthal to radial polarisation (depicted by blue triangles). Radial polarisation is composed as $\text{TEM}_{01(x)}\hat{e}_x + \text{TEM}_{01(y)}\hat{e}_y$ (Nesterov & Niziev 2000; Oron *et al*. 2000).

https://doi.org/10.1017/S0022377825101062 Published online by Cambridge University Press

Figure 5(*a*) shows the evolution of the mean electron angular momentum $\langle p_\theta \rangle$, which exhibits oscillations with increasing amplitude, consistent with the etching-driven dynamics discussed around figures 2 and 4. Given the multidimensional structure and transverse focusing fields, the electrons also undergo betatron oscillations with a frequency $\omega_\beta = \omega_p/\sqrt{2\gamma}$ (Tajima & Dawson 1979; Esarey, Schroeder & Leemans 2009), as observed in the radial momentum $\langle p_r \rangle$ in figure 5(*b*). The longitudinal momentum $\langle p_z \rangle$ increases steadily before eventually saturating, as shown in figure 5(*c*). Adjustments to laser parameters influence the polarity, magnitude and distribution of angular (transverse) momentum of the injected electrons. In figure 5(*a*), we see that varying the laser's initial phase influences the polarity of the angular momentum $\langle p_\theta \rangle$, but has no influence on the radial and axial momentum. Reducing the laser-to-plasma frequency ratio impacts the oscillation period and magnitude of the angular momentum, due to the increased etching velocity $v_{\text{etch}} \approx c(\omega_p^2/\omega_0^2)$. It also allows for increased angular momentum, but the longitudinal momentum saturates more quickly. This can be seen in figure 5(*c*). However, radial polarisation does not lead to the angular motion, but introduces significant modifications to the radial momentum $\langle p_r \rangle$, adding a distinct modulation on top of the betatron oscillations, which becomes prominent as pump depletion progresses ($t > 120/\omega_p$), as shown in figure 5(*b*). Experimental diagnostics of this mechanism could rely on the rotating high-energy electrons, which emit betatron radiation with spatial or polarisation features that reflect their angular momentum (Luís Martins *et al*. 2019). While this effect was not modelled in our simulations, the resulting X-rays could be measured using standard betatron radiation diagnostics (Phuoc *et al*. 2006; Corde *et al*. 2013; Thaury *et al*. 2013).

Additionally, the electromagnetic field structure from the downshifted azimuthally polarised laser fields, particularly E_θ, B_r and B_z, inside the bubble is orthogonal to that of conventional wakefields, offering a measurable signature, for example, via electron probing (Zhang *et al*. 2016; Raj *et al*. 2020; Wan *et al*. 2024).

4. Conclusions

In conclusion, we demonstrated that plasma electrons and ions can acquire substantial angular momentum via canonical momentum conservation, driven by a high-intensity azimuthally polarised laser pulse undergoing local pump depletion in underdense plasma. Through a combination of analytical considerations and particle-in-cell simulations, we explored the mechanism of transverse momentum gain of electrons in one-dimensional scenarios and extended our analysis to three dimensions, obtaining consistent results. This mechanism relies on local pump depletion of the laser pulse, which facilitates the development of a long-wavelength offset in the vector potential trailing the pulse. This offset enables the rotation of the wakefield's sheath currents and the self-injected electrons. The highest-energy electrons exhibit angular momentum with a small spread and undergo characteristic oscillations linked to the erosion of the laser pulse front. We found that the angular momentum gained by the electrons is compensated by that of the ions and the combined fields of the laser and the nonlinear plasma wave. Finally, we highlighted the controllability of angular and transverse momentum gain under local pump depletion by varying key laser parameters, including the initial phase, laser-to-plasma frequency ratio and polarisation. A more systematic parametric study, including variations in laser pulse shape and intensity, and electron density, would help further characterise the robustness and scaling of this mechanism regarding potential experimental realisation, and is left for future work.

https://doi.org/10.1017/S0022377825101062 Published online by Cambridge University Press

Future work will also aim to test the limits of this scheme, explore exotic laser polarisations, investigate radiation emitted by high-energy electrons and incorporate ionisation effects. Finally, the presented mechanism potentially impacts set-ups involving lasers with angular momentum, such as circularly polarised Gaussian and Laguerre–Gaussian beams, which merits further investigation.

Acknowledgements

We would like to acknowledge the anonymous reviewer for their valuable and constructive comments, which helped us to improve the quality of this work. The authors used AI tools to assist with copy editing (improvements on readability and style, and to ensure that the texts are free of errors in grammar, spelling and punctuation).

Editor Victor Malka thanks the referees for their advice in evaluating this article.

Funding

We gratefully acknowledge EuroHPC for awarding us access to LUMI-C at CSC (Finland) and FCT (Portugal) for access to Marenostrum V at the Barcelona Supercomputer Center [https://doi.org/10.54499/2024.06987.CPCA.A3]. This work was supported by the EuPRAXIA-PP under grant agreement No. 101079773 and FCT under the projects No. X-MASER-2022.02230. PTDC [https://doi.org/10.54499/2022.02230.PTDC], UID/FIS/50010/2025 [https://doi.org/10.54499/UID/50010/2025], and IPFN-CEEC-INST-LA3/IST-ID [https://doi.org/10.54499/LA/P/0061/2020]. This work was also supported by la Caixa' Foundation (ID 100010434), under fellowship code LCF/BQ/DI19/11730025.

Supplementary movie

Supplementary movie is available at https://doi.org/10.1017/S0022377825101062.

Declaration of interests

The authors report no conflict of interest.

Appendix. Angular momentum conservation

The Lagrangian for an electron in an electromagnetic wave in a wakefield can be written as (Jackson 1998)

$$L = -m_e c^2 \left(1 - \frac{\boldsymbol{v}\cdot\boldsymbol{v}}{c^2}\right)^{1/2} + \frac{e}{c}\boldsymbol{v}\cdot\boldsymbol{A} - e\phi, \tag{A1}$$

where $\boldsymbol{v}$ is the velocity vector, c is the speed of light, $\boldsymbol{A}$ is the laser's vector potential, ϕ is the scalar potential (here, the wakefield potential), and m_e, e are the electron's mass and charge, respectively. Our system is cylindrically symmetric and, for this purpose, we write the Lagrangian in cylindrical coordinates as

$$L = -m_e c^2 \left(1 - \frac{\dot{z}^2}{c^2} - \frac{r^2\dot{\theta}^2}{c^2} - \frac{\dot{r}^2}{c^2}\right)^{1/2} - e\left(\dot{z}A_z + r\dot{\theta}A_\theta + \dot{r}A_r\right) + e\phi, \tag{A2}$$

where $\dot{z} = dz/dt$ is the axial velocity, $\dot{\theta} = d\theta/dt$ is the angular velocity and $\dot{r} = dr/dt$ is the radial velocity. To determine whether angular momentum is conserved in this

https://doi.org/10.1017/S0022377825101062 Published online by Cambridge University Press

system, we calculate the generalised angular momentum

$$P_\theta = \frac{\partial L}{\partial \dot{\theta}} = m_e \gamma r^2 \dot{\theta} - eA_\theta r, \tag{A3}$$

where $\gamma = 1/\sqrt{1-(\dot{z}^2 + r^2\dot{\theta}^2 + \dot{r}^2)/c^2}$. Here, $m_e\gamma r\dot{\theta} = p_\theta$ is the azimuthal momentum and there is no angular velocity dependence on the wakefield potential, i.e. $\partial\phi/\partial\dot{\theta} = 0$. The generalised angular momentum is conserved when the Hamiltonian, given by

$$H = \sqrt{(c\boldsymbol{P} - e\boldsymbol{A})^2 + m_e^2c^4} + e\phi, \tag{A4}$$

has no angular dependence, i.e.

$$\frac{\mathrm{d}P_\theta}{\mathrm{d}t} = -\frac{\partial H}{\partial \theta} = 0. \tag{A5}$$

This results in $P_\theta = 0$, because there is no initial angular momentum in the system, such that $p_\theta = eA_\theta$.

This condition holds for a cylindrical vector beam with azimuthal polarisation, where the laser pulse has no angular dependence and the vector potential has only an azimuthal component, $\boldsymbol{A} = A_\theta(r, z)\hat{e}_\theta$, where at focus, $A(r, 0)_\theta = a_0(r/w_0)\exp(-r^2/w_0^2)$. In this case, plasma electrons can only acquire angular momentum through canonical momentum conservation, $p_\theta = eA_\theta$.

REFERENCES

ALI, S., DAVIES, J.R. & MENDONCA, J.T. 2010 Inverse faraday effect with linearly polarized laser pulses. *Phys. Rev. Lett.* **105**, 035001.

ALLEN, L., BEIJERSBERGEN, M.W., SPREEUW, R.J.C. & WOERDMAN, J.P. 1992 Orbital angular momentum of light and the transformation of Laguerre–Gaussian laser modes. *Phys. Rev. A* **45**, 8185.

BAUMANN, C. & PUKHOV, A. 2018 Electron dynamics in twisted light modes of relativistic intensity. *Phys. Plasmas* **25**, 083114.

BULANOV, S.V., INOVENKOV, I.N., KIRSANOV, V.I., NAUMOVA, N.M. & SAKHAROV, A.S. 1992 Nonlinear depletion of ultrashort and relativistically strong laser pulses in an underdense plasma. *Phys. Fluids B* **4**, 1935–1942.

CHEN, Z.Y. & PUKHOV, A. 2015 High field terahertz emission from relativistic laser-driven plasma wakefields. *Phys. Plasmas* **22**, 103105.

CORDE, S., THAURY, C., LIFSCHITZ, A., LAMBERT, G., TA PHUOC, K., DAVOINE, X., LEHE, R., DOUILLET, D., ROUSSE, A. & MALKA, V. 2013 Observation of longitudinal and transverse self-injections in laser-plasma accelerators. *Nat. Commun.* **4**, 1501.

DECKER, C.D., MORI, W.B., TZENG, K.-C. & KATSOULEAS, T. 1996 The evolution of ultra-intense, short-pulse lasers in underdense plasmas. *Phys. Plasmas* **3**, 2047–2056.

DIAS, J.M., SILVA, L.O. & MENDONÇA, J.T. 1998 Photon acceleration versus frequency-domain interferometry for laser wakefield diagnostics. *Phys. Rev. Accel. Beams* **1**, 031301.

DOWNER, M.C., ZGADZAJ, R., DEBUS, A., SCHRAMM, U. & KALUZA, M.C. 2018 Diagnostics for plasma-based electron accelerators. *Rev. Mod. Phys.* **90**, 035002.

ESAREY, E., SCHROEDER, C.B. & LEEMANS, W.P. 2009 Physics of laser-driven plasma-based electron accelerators. *Rev. Mod. Phys.* **81**, 1229–1285.

ESAREY, E., SPRANGLE, P., KRALL, J. & TING, A. 1996 Overview of plasma-based accelerator concepts. *IEEE Trans. Plasma Sci.* **24**, 252–288.

FAURE, J., GLINEC, Y., SANTOS, J.J., EWALD, F., ROUSSEAU, J.-P., KISELEV, S., PUKHOV, A., HOSOKAI, T. & MALKA, V. 2005 Observation of laser-pulse shortening in nonlinear plasma waves. *Phys. Rev. Lett.* **95**, 205003.

https://doi.org/10.1017/S0022377825101062 Published online by Cambridge University Press

FONSECA, R.A. *et al.* 2002 Osiris: a three-dimensional, fully relativistic particle in cell code for modeling plasma based accelerators. In *Computational Science – ICCS 2002: International Conference Amsterdam, The Netherlands, April 21–24, 2002 Proceedings, Part III*, vol. 2, p. 24. Springer.

FROLOV, A.A. 2004 Excitation of magnetic fields by a circularly polarized laser pulse in a plasma channel. *Plasma Phys. Rep.* **30**, 698–709.

GORBUNOV, L.M. & RAMAZASHVILI, R.R. 1998 Magnetic field generated in a plasma by a short, circularly polarized laser pulse. *J. Exp. Theor. Phys.* **87**, 461–467.

GORDON, D.F., HAFIZI, B., HUBBARD, R.F., PENANO, J.R., SPRANGLE, P. & TING, A. 2003 Asymmetric self-phase modulation and compression of short laser pulses in plasma channels. *Phys. Rev. Lett.* **90**, 215001.

HAINES, M.G. 2001 Generation of an axial magnetic field from photon spin. *Phys. Rev. Lett.* **87**, 135005.

JACKSON, J.D. 1998 *Classical Electrodynamics*, 3rd edn. Wiley.

KATOH, M., FUJIMOTO, M., KAWAGUCHI, H., TSUCHIYA, K., OHMI, K., KANEYASU, T., TAIRA, Y., HOSAKA, M., MOCHIHASHI, A. & TAKASHIMA, Y. 2017 Angular momentum of twisted radiation from an electron in spiral motion. *Phys. Rev. Lett.* **118**, 094801.

KOSTYUKOV, I., SHVETS, G., FISCH, N.J. & RAX, J.M. 2001 Inverse Faraday effect in a relativistic laser channel. *Laser Part. Beams* **19**, 133–136.

LIU, W., JIA, Q. & ZHENG, J. 2023 Inverse faraday effect of weakly relativistic full poincaré beams in plasma. *Matter Radiat. Extrem.* **8**, 014405.

LONGMAN, A. & FEDOSEJEVS, R. 2021 Kilo-Tesla axial magnetic field generation with high intensity spin and orbital angular momentum beams. *Phys. Rev. Res.* **3**, 043180.

LU, Y. *et al.* 2021 Ultra-brilliant gev betatronlike radiation from energetic electrons oscillating in frequency-downshifted laser pulses. *Opt. Express* **29**, 8926–8940.

LUÍS MARTINS, J., VIEIRA, J., FERRI, J. & FÜLÖP, T. 2019 Radiation emission in laser-wakefields driven by structured laser pulses with orbital angular momentum. *Sci. Rep.* **9**, 9840.

MENDONÇA, J.T. & SILVA, L.O. 1994 Regular and stochastic acceleration of photons. *Phys. Rev. E* **49**, 3520.

MORI, W.B. 1997 The physics of the nonlinear optics of plasmas at relativistic intensities for short-pulse lasers. *IEEE J. Quantum Electron.* **33**, 1942–1953.

MURPHY, C.D. *et al.* 2006 Evidence of photon acceleration by laser wake fields. *Phys. Plasmas* **13**, 033108.

NAJMUDIN, Z. *et al.* 2001 Measurements of the inverse faraday effect from relativistic laser interactions with an underdense plasma. *Phys. Rev. Lett.* **87**, 215004.

NASERI, N., BYCHENKOV, V.YU & ROZMUS, W. 2010 Axial magnetic field generation by intense circularly polarized laser pulses in underdense plasmas. *Phys. Plasmas* **17**, 083109.

NERUSH, E.N. & KOSTYUKOV, I.Y. 2009 Carrier-envelope phase effects in plasma-based electron acceleration with few-cycle laser pulses. *Phys. Rev. Lett.* **103**, 035001.

NESTEROV, A.V. & NIZIEV, V.G. 2000 Laser beams with axially symmetric polarization. *J. Phys. D: Appl. Phys.* **33**, 1817–1822.

NIE, Z. *et al.* 2020 Photon deceleration in plasma wakes generates single-cycle relativistic tunable infrared pulses. *Nat. Commun.* **11**, 2787.

NUTER, R., KORNEEV, PH, DMITRIEV, E., THIELE, I. & TIKHONCHUK, V.T. 2020 Gain of electron orbital angular momentum in a direct laser acceleration process. *Phys. Rev. E* **101**, 053202.

ORON, R., BLIT, S., DAVIDSON, N., FRIESEM, A.A., BOMZON, Z. & HASMAN, E. 2000 The formation of laser beams with pure azimuthal or radial polarization. *Appl. Phys. Lett.* **77**, 3322–3324.

PAI, C. *et al.* 2010 Generation of intense ultrashort midinfrared pulses by laser-plasma interaction in the bubble regime. *Phys. Rev. A.* **82**, 063804.

PHUOC, K.T., CORDE, S., SHAH, R., ALBERT, F., FITOUR, R., ROUSSEAU, J.-P., BURGY, F., MERCIER, B. & ROUSSE, A. 2006 Imaging electron trajectories in a laser-wakefield cavity using betatron x-ray radiation. *Phys. Rev. Lett.* **97**, 225002.

PORFIREV, A., KHONINA, S. & KUCHMIZHAK, A. 2023 Light–matter interaction empowered by orbital angular momentum: control of matter at the micro-and nanoscale. *Prog. Quantum Electron.* **88**, 100459.

PUKHOV, A. & MEYER-TER VEHN, J. 2002 Laser wake field acceleration: the highly non-linear broken-wave regime. *Appl. Phys. B* **74**, 355–361.

https://doi.org/10.1017/S0022377825101062 Published online by Cambridge University Press

RAJ, G. *et al.* 2020 Probing ultrafast magnetic-field generation by current filamentation instability in femtosecond relativistic laser-matter interactions. *Phys. Rev. Res.* **2**, 023123.

SABERI, H., VIEIRA, J. & SILVA, L.O. 2017 Ponderomotive beatwave ion acceleration using twisted light. *Phys. Plasmas* **24**, 103131.

SCHREIBER, J., BELLEI, C., MANGLES, S.P.D., KAMPERIDIS, C., KNEIP, S., NAGEL, S.R., PALMER, C.A.J., RAJEEV, P.P., STREETER, M.J.V. & NAJMUDIN, Z. 2010 Complete temporal characterization of asymmetric pulse compression in a laser wakefield. *Phys. Rev. Lett.* **105**, 235003.

SEIPT, D., SURZHYKOV, A. & FRITZSCHE, S. 2014 Structured x-ray beams from twisted electrons by inverse compton scattering of laser light. *Phys. Rev. A* **90**, 012118.

SHENG, Z.M. & MEYER-TER VEHN, J. 1996 Inverse faraday effect and propagation of circularly polarized intense laser beams in plasmas. *Phys. Rev. E* **54**, 1833–1842.

SHI, Y., VIEIRA, J., TRINES, R.M.G.M., BINGHAM, R., SHEN, B.F. & KINGHAM, R.J. 2018 Magnetic field generation in plasma waves driven by copropagating intense twisted lasers. *Phys. Rev. Lett.* **121**, 145002.

SHIRAISHI, S. *et al.* 2013 Laser red shifting based characterization of wakefield excitation in a laser-plasma accelerator. *Phys. Plasmas* **20**, 063103.

SILVA, L.O. & MENDONÇA, J.T. 1998 Kinetic theory of photon acceleration: time-dependent spectral evolution of ultrashort laser pulses. *Phys. Rev. E* **57**, 3423.

SILVA, L.O. & MENDONÇA, J.T. 2001 Photon kinetic theory of self-phase modulation. *Opt. Commun.* **196**, 285–291.

TAJIMA, T. & DAWSON, J.M. 1979 Laser electron accelerator. *Phys. Rev. Lett.* **43**, 267.

TALIN, B., KAFTANDJIAN, V.P. & KLEIN, L. 1975 Inverse Faraday effect in plasmas. *Phys. Rev. A* **11**, 648–657.

THAURY, C., GUILLAUME, E., CORDE, S., LEHE, R., LE BOUTEILLER, M., TA PHUOC, K., DAVOINE, X., RAX, J.M., ROUSSE, A. & MALKA, V. 2013 Angular-momentum evolution in laser-plasma accelerators. *Phys. Rev. Lett.* **111**, 135002.

TSUNG, F.S., REN, C., SILVA, L.O., MORI, W.B. & KATSOULEAS, T. 2002 Generation of ultra-intense single-cycle laser pulses by using photon deceleration. *Proc. Natl Acad. Sci. USA* **99**, 29–32.

VIEIRA, J., FIÚZA, F., SILVA, L.O., TZOUFRAS, M. & MORI, W.B. 2010 Onset of self-steepening of intense laser pulses in plasmas. *New J. Phys.* **12**, 045025.

VIEIRA, J. & MENDONÇA, J.T. 2014 Nonlinear laser driven donut wakefields for positron and electron acceleration. *Phys. Rev. Lett.* **112**, 215001.

VIEIRA, J., MENDONÇA, J.T. & QUÉRÉ, F. 2018 Optical control of the topology of laser-plasma accelerators. *Phys. Rev. Lett.* **121**, 054801.

VOLKE-SEPULVEDA, K., GARCES-CHAVEZ, V., CHAVEZ-CERDA, S., ARLT, J. & DHOLAKIA, K. 2002 Orbital angular momentum of a high-order Bessel light beam. *J. Opt. B: Quantum Semiclass. Opt.* **4**, S82.

WAN, Y., TATA, S., SEEMANN, O., LEVINE, E.Y., KROUPP, E. & MALKA, V. 2024 Real-time visualization of the laser-plasma wakefield dynamics. *Sci. Adv.* **10**, eadj3595.

ZHANG, C.J. *et al.* 2016 Capturing relativistic wakefield structures in plasmas using ultrashort high-energy electrons as a probe. *Sci. Rep.* **6**, 29485.

ZHU, W., PALASTRO, J.P. & ANTONSEN, T.M. 2012 Studies of spectral modification and limitations of the modified paraxial equation in laser wakefield simulations. *Phys. Plasmas* **19**, 033105.

ZHU, W., PALASTRO, J.P. & ANTONSEN, T.M. 2013 Pulsed mid-infrared radiation from spectral broadening in laser wakefield simulations. *Phys. Plasmas* **20**, 073103.

ZHU, X., WENG, S., CHEN, M., SHENG, Z. & ZHANG, J. 2020 Efficient generation of relativistic near-single-cycle mid-infrared pulses in plasmas. *Light: Sci. Appl.* **9**, 46.

https://doi.org/10.1017/S0022377825101062 Published online by Cambridge University Press